SCIENCE CHINA
Information Sciences

• RESEARCH PAPER •

April 2025, Vol. 68, Iss. 4, 140405:1–140405:10
https://doi.org/10.1007/s11432-024-4194-9

Special Topic: Photonics Technology

High quantum efficiency ultraviolet photodetector based on graphene and truncated silicon nanocones

Feng TIAN[1,2,3], Shaoxiong WU[1,2], Xinyu LIU[2], Baoshi QIAO[1], Dong PU[1,2], Zongwen LI[2], Cheng CHEN[1], Xiaoxue CAO[2], Srikrishna Chanakya BODEPUDI[2], Muhammad Abid ANWAR[2], Xiaochen WANG[2], Yuda ZHAO[2], Bin YU[2], Tawfique HASAN[3*], Huan HU[1,2*] & Yang XU[1,2*]

[1]*ZJU-UIUC Institute, International Campus, Zhejiang University, Haining 314400, China*
[2]*College of Integrated Circuits, ZJU-Hangzhou Global Scientific and Technological Innovation Center, Zhejiang University, Hangzhou 310027, China*
[3]*Cambridge Graphene Centre, University of Cambridge, Cambridge CB3 0FA, UK*

Received 24 April 2024/Revised 27 July 2024/Accepted 18 October 2024/Published online 27 February 2025

Abstract Ultraviolet photodetectors have a wide range of applications, covering optical analysis, environmental detection, and security solutions. While silicon is extensively used in photodetection, the performance of silicon-based photodetectors in the ultraviolet spectrum is poorer compared to that in the visible range due to limited absorption depth and high reflectivity. To enhance its ultraviolet sensing capabilities, a graphene/truncated silicon cones heterostructure-based photodetector is proposed to simultaneously increase the light-trapping effect and create ultra-shallow Schottky junctions. The design reduces the reflectivity to <12% in the ultraviolet (UV) range, less than 20% of the original value. The graphene/truncated silicon cone photodetectors can achieve responsivity and external quantum efficiency that exceed 0.32 A/W and 113% at a wavelength of 360 nm, respectively. By analyzing the experimental and simulation results, it is confirmed that the elevated performance is a consequence of the combined effects of light-trapping, shallow junction, and impact ionization. Our approach in combining graphene with nanostructured silicon shows promise in future large-scale CMOS integration and high-performance optoelectronic applications.

Keywords silicon, graphene, ultraviolet photodetector, truncated cones, nanostructures

Citation Tian F, Wu S X, Liu X Y, et al. High quantum efficiency ultraviolet photodetector based on graphene and truncated silicon nanocones. Sci China Inf Sci, 2025, 68(4): 140405, https://doi.org/10.1007/s11432-024-4194-9

1 Introduction

Ultraviolet (UV) photodetectors play a critical role in acquiring and analyzing UV light information within the 10–400 nm wavelength range, manifesting a broad spectrum of applications encompassing environmental monitoring, flame detection, and biological analysis [1–6]. Wide bandgap semiconductors, such as GaN, ZnO, and SiC, are currently used for constructing UV photodetectors but still suffer from the intricate challenges in material growth, device fabrication, and integration with CMOS technology [3, 7–12]. Silicon, on the other hand, presents several advantages in photodetection. It offers a diverse range of photodetection mechanisms and device structures, such as PN and Schottky junctions, and benefits from a highly-matured mass-manufacturing platform. However, high reflectivity and low absorption depth of silicon in the UV range are two bottlenecks, severely limiting its performance in UV detection [8]. Absorption depth reflects the electromagnetic wave penetration into a material. It is defined as the distance at which the intensity or power of the electromagnetic field decays to 1/e of its original value at the material's surface [13]. In the UV range, the absorption depth of silicon is less than 100 nm and drops to below 10 nm before reaching a wavelength of 360 nm [14, 15]. When the photodetector junction is positioned deeper than the absorption depth, most absorbed light does not effectively contribute to the photocurrent, leading to low responsivity. Therefore, shallow PN and Schottky junctions have been extensively investigated [3, 16]. Nevertheless, PN junctions commonly exhibit large depth and

* Corresponding author (email: th270@cam.ac.uk, huanhu@intl.zju.edu.cn, yangxu-isee@zju.edu.cn)

are accompanied by a dead layer, which can adversely affect the photodetection performance of UV photodetection [3]. Schottky junctions are typically formed by combining silicon with a thin metal or a graphene layer [3, 8, 17–22]. Compared to thin metal, graphene stands out due to its atomic thinness and over 90% transparency in ultraviolet, making it a promising choice for forming ultra-shallow junctions with silicon.

To address the high reflectivity of silicon, researchers have explored silicon structures with different morphologies and dimensions to reduce the reflection [23–38]. Indeed, both morphologies and dimensions significantly influence the performance of photodetectors. Photodetectors based on micrometer-scale silicon structures are generally well-suited for the detection of near-infrared light [23–25], while nanometer-scale silicon structures are usually suitable for the detection of broadband [26–30, 35–37] or shorter wavelengths [32, 38]. The variations in the detection performance of detectors resulting from structures of different morphologies are based on distinct principles. For instance, silicon nanowires with a diameter of 45 nm exhibit the potential for visible-blind UV detection due to leaky mode resonance [38]. On the other hand, cone-like shape silicon PN junctions can be harnessed for UV detection by facilitating multiple carrier generation [39]. The utilization of truncated cones for visible and near-infrared detection was attributed to their light-trapping effect [26]. The approaches provide evidence that cone-like nanostructures have the potential to demonstrate better performance than nanopillars.

Here, we employ truncated silicon nanocones with graphene to fabricate high-performance ultraviolet photodetectors by reducing the reflectivity and simultaneously using the shallow Schottky junction between graphene and silicon. Our findings demonstrate that the photo-responsivity of graphene/truncated silicon cones (G-TSC)-based photodetectors exceed 0.32 A/W, with a corresponding external quantum efficiency (EQE) of >113% at 360 nm wavelength aided by impact ionization within the silicon nanostructures. Crucially, our use of nanosphere lithography in the truncated nanocone fabrication eliminates the need for e-beam lithography, significantly reducing the costs while opening opportunities for scalable commercial fabrication.

2 Results and discussion

Figure 1(a) shows the fabrication process of G-TSC ultraviolet photodetectors. Multiple 2 mm × 2 mm silicon windows were defined by UV-lithography and etched by buffered oxide etchant (BOE) on a silicon wafer (Figure 1(b)). Next, a monolayer of polystyrene (PS) nanospheres (400 nm in diameter) was deposited on the wafer to serve as masks, which is known as nanosphere lithography [40–42]. Oxygen plasma was used to etch PS nanospheres to the desired size (∼350 nm). Subsequently, various truncated silicon cones are fabricated by inductively coupled plasma (ICP) etching with SF_6 and C_4F_8. After the fabrication of gold electrodes using sputtering, a monolayer graphene grown by chemical vapor deposition (CVD) was transferred to the devices [8].

We fabricated three kinds of G-TSC photodetectors and a control group with graphene/flat silicon. With an increase in etching time, the top diameter of the truncated cones decreases while their height increases (Figure S1). As shown in Figures 1(e)–(g), the truncated silicon cones are clean and uniform. The geometry of these devices is shown in inset figures, which are measured and analyzed by scanning electron microscope (SEM) images. Figure 1(c) is an SEM image of monolayer CVD graphene transferred onto truncated silicon cones without obvious damage.

Figure 1(d) shows the measured reflectivity spectrum of these truncated silicon cones, while Figure S2 showcases the corresponding simulation results. The first observation is that the reflectivity of truncated silicon cones increases with their depth. This trend is consistently observed both in simulation and experimental results. However, it is essential to note that the experimental reflectivity values are higher than those predicted by the simulations for all wavelengths. This discrepancy is attributed to the imperfections in the periodicity of the fabrication process, which the simulations may not fully reflect. The significant reduction of reflectivity is due to the light trapping effect [27, 35].

In Figure 2(a), we presented the current vs. voltage (I-V) curve of the G-TSC (H = 720 nm) junction, both in the dark and under exposure to 375 nm UV light. It shows a relatively low dark current (<10 nA) and a dramatic gain (>3 orders) in current from UV light. The band diagram of the G-TSC photodetector is shown in Figure 2(b), which could explain the working principle. When the device is illuminated by ultraviolet light, most of the incident light is absorbed by silicon, resulting in the generation of photogenerated carriers near the silicon surface. These photogenerated carriers are then effectively

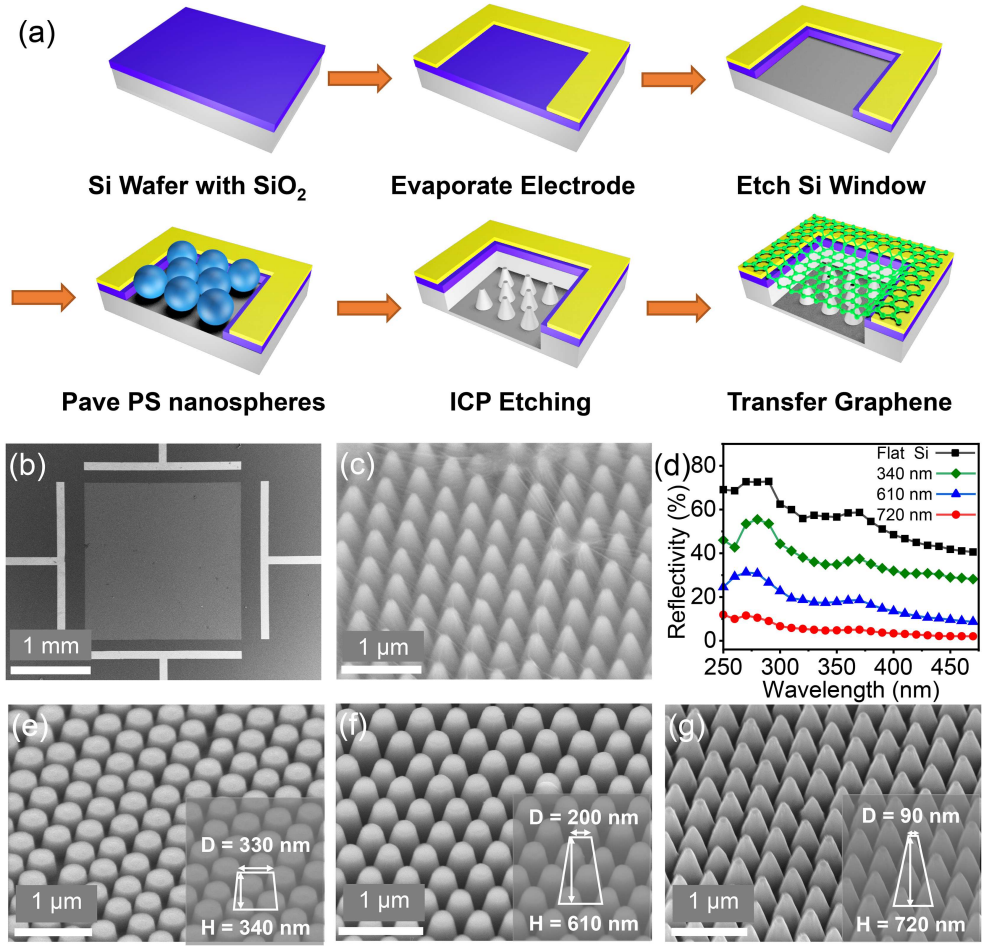

Figure 1 (Color online) Fabrication process and scanning electron microscope (SEM) images. (a) Overview of the fabrication process for G-TSC ultraviolet photodetectors; (b) top view SEM image of the photodetector; (c) oblique view (45°) SEM images of graphene and truncated silicon cone with 720 nm in height (H); (d) the measured reflectivity of flat silicon and different truncated silicon cones; oblique view (45°) SEM images of truncated silicon cones with (e) 340 nm, (f) 610 nm, and (g) 720 nm in height (H), respectively.

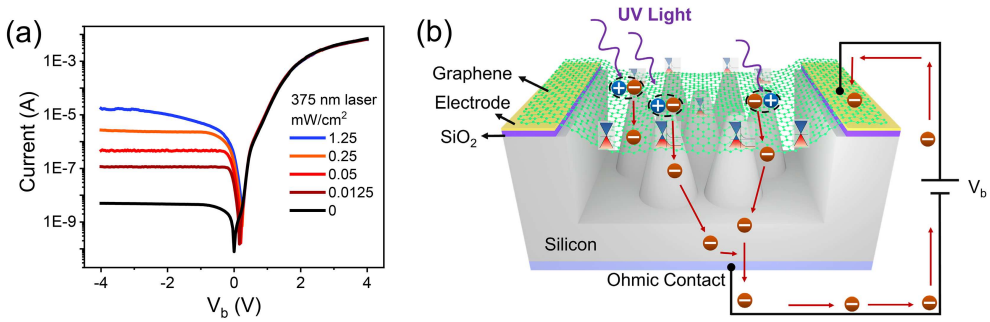

Figure 2 (Color online) Photoresponse mechanism. (a) The current vs. voltage (I-V) characteristics of the device (H = 720 nm) in darkness and under the illumination of 375 nm UV light. The effective area is 4 mm^2. (b) The 3-dimensional schematic diagram combined with the energy band diagram of the G-TSC.

separated at the depletion region. At the same time, graphene also absorbs a fraction of incident light, and the photo-excited electrons will cross the Schottky barrier (internal photoemission) and be collected by silicon [43–45]. The reduction of the reflectivity of the device by nanostructures, coupled with the ultra-shallow Schottky junction, will contribute to improving the performance of silicon-based ultraviolet photodetectors.

To investigate the wavelength-dependent response of G-TSC photodetectors, we conducted current

measurements from 250 to 750 nm. The photo-responsivity and external quantum efficiency are extracted as shown in Figure S3(a) and Figure 3(a).

Within the ultraviolet range, the responsivity and EQE of G-TSC structures outperform graphene/flat silicon structures. This enhancement primarily stems from the reduction of reflection, i.e., the increment of absorption in the ultraviolet range. Under these conditions, the rejection ratio (360 nm/500 nm) of G-TSC (H = 720 nm) could be extracted as 40.7, while the rejection ratios for other structures are 5.2 for G-TSC (H = 610 nm) and 3.2 for G-TSC (H = 340 nm).

The observed EQE of the device at specific ultraviolet wavelengths exceeds 100%, an effect attributed to the impact ionization process. Experimental observations and theoretical calculations both suggest that a substantial rise in the quantum yield takes place at approximately three times the bandgap energy (E_g), i.e., 3.3 eV for silicon at room temperature [39, 46–50].

To investigate the underlying factors further and eliminate the influence of reflectivity, we have determined the internal quantum efficiency (IQE) of graphene/flat silicon and G-TSC (H = 720 nm) devices. The IQE is calculated as IQE = EQE/(1−Reflectivity), and the results are depicted in Figure 3(b). There are two peaks of both graphene/flat silicon devices and graphene/truncated silicon cone devices.

These peaks are at around 4.3 eV (label A, ∼288 nm) and 3.4 eV (label B, ∼365 nm), and can be correlated to impact ionization by hot holes and hot electrons generated through the transitions within the silicon band structure [39, 51].

Although the structured devices exhibit higher EQE, an interesting contrast emerges with their IQE being lower compared to planar devices. This can be attributed to the truncated cone structures, bringing lower reflection, recombination sites, and longer distances for diffusion. The carrier recombination sites come from ICP-induced damages (mainly on sidewalls) [52–55], larger surface areas with different orientations, etc. [39].

For a more comprehensive understanding, we created a three-dimensional model of the truncated silicon cones within the hexagonal prism unit, employing the parameters depicted in Figure 1. We conducted a finite element analysis simulation under the illumination of light (λ = 300, 500, 700 nm). The electric field distribution inside the silicon of different structures is shown in Figure 3(c). In both the structured and flat silicon configurations, most of the electric field is concentrated at the top surface of the silicon structure. In particular, the electric field strength is significantly higher in truncated silicon cones compared to flat silicon. This result also explains the high quantum efficiency of G-TSC.

While the absorption and simulated electric field distribution of G-TSC remain robust in the visible range, as indicated in Figure 3(c), the responsivity and EQE of graphene/truncated silicon cone structures are relatively lower compared to those of the graphene/flat silicon configuration within the visible range (Figure S3(a) and Figure 3(a)). The possible reason is that the absorption depth of silicon in the visible range is much larger than that in the ultraviolet range. Thus, most of the photogenerated carriers could not be separated effectively in the depletion region because the defects of sidewalls of truncated cones largely reduce the lifetime of photogenerated carriers. In other words, the recombination is more significant in the visible range because of a more considerable absorption depth.

We also note that the extracted Schottky barrier heights of graphene/flat silicon, G-TSC (H = 340, 610, 720 nm) are 0.678, 0.613, 0.622, and 0.656 eV (Figure S4), respectively [56]. The barrier height represents the difference between the work function of graphene and the electron affinity of silicon [13]. It quantifies the energy barrier that charge carriers must overcome to traverse the junction.

There are two possible reasons for the difference in Schottky barrier height. Firstly, the Fermi level of graphene is changed by dopant induced by different contact areas of silicon or strain caused by silicon structures [57–68]. Secondly, the interfacial layer of silicon and graphene reduces the barrier height. More specifically, the interfacial layer accounts for the dry etching-induced damage [52–55], the residue of PS nanosphere, and the different thicknesses of oxide layer [20, 69, 70] on different silicon structures. It is important to note that the effective area is the top of the truncated silicon cones, which is protected by PS nanospheres during the etching step. However, the nanospheres are not able to withstand the isotropic etching process completely, leading to damage to the silicon surface. The possible residue of nanospheres is another possible source to affect the sidewall surface. Finally, the difference in thickness of the oxide layer [69] on various silicon structures may also contribute to the variation in the barrier height. We suggest that these two reasons may coexist simultaneously, enhancing the overall variation.

Furthermore, we conducted Raman spectroscopy on graphene to investigate the factors contributing to the variance in barrier heights (Figure 4(a)). The G peak of graphene on flat silicon, truncated silicon cones (H = 340, 610, and 720 nm) is 1588.7 ± 1, 1586.7 ± 0.3, 1584.6 ± 0.2, and 1584.0 ± 0.2 cm^{-1},

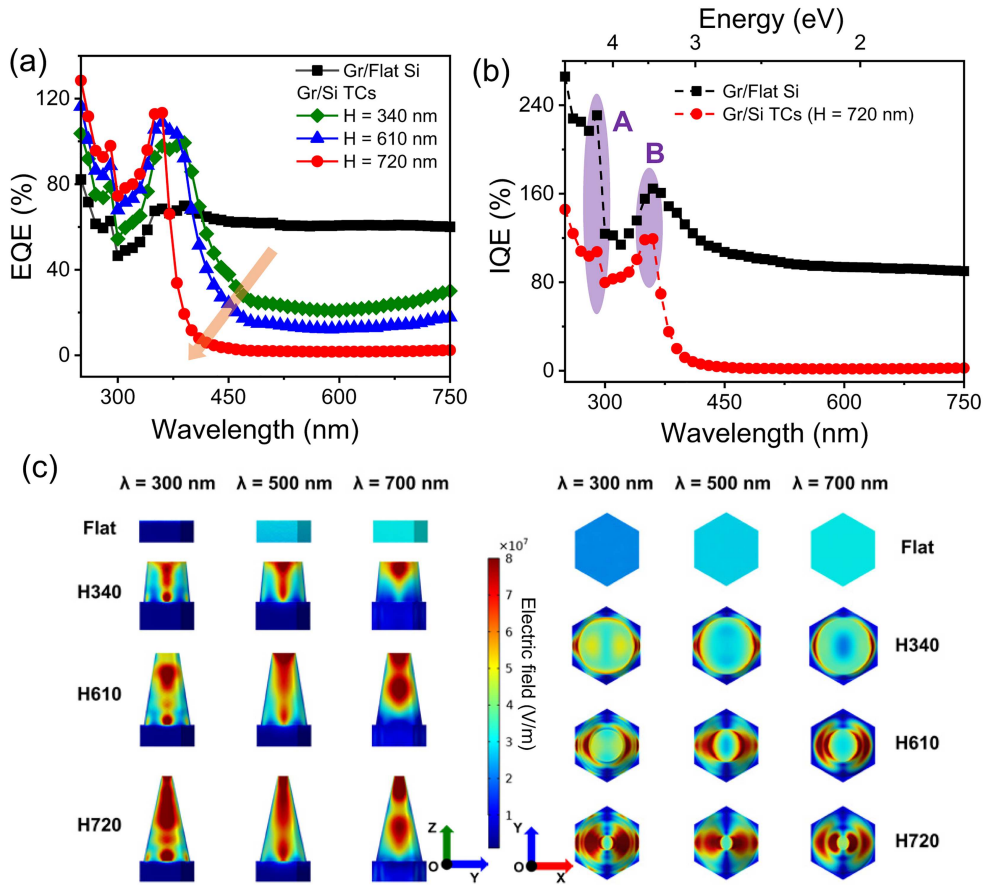

Figure 3 (Color online) Wavelength-dependent response. (a) External quantum efficiency vs. λ of different devices; (b) the internal quantum efficiency of graphene/flat silicon and graphene/truncated silicon cones (H = 720 nm); (c) simulated electric field distribution (xoy and yoz) of different silicon structures by illumination with light (λ = 300, 500, 700 nm).

respectively. And the 2D peak is 2686.7 ± 0.3, 2678.0 ± 0.1, 2675.7 ± 0.1, and 2674.7 ± 0.1 cm^{-1}, respectively. Notably, there are observable shifts in both the G and 2D peaks across these different structures, which is related to the potential strain and dopant effect.

Since the size of the light spot in the Raman system is considerably larger than the dimensions of nanostructures, the Raman signal provides an average result encompassing both suspended graphene and graphene on silicon. To investigate the structural details and electrical potential on the nanoscale, we employed atomic force microscopy (AFM) and Kelvin probe force microscopy (KPFM) techniques. A new device with truncated silicon nanocones, half of which is covered with graphene, is prepared to compare the difference (Figure 4(b)). By analyzing the potential difference between silicon, suspended graphene, and graphene on silicon (Figures 4(c) and (d)). Two observations are noted from the experiments. First, the potential of silicon is larger than that of graphene, which is consistent with the data in Figure 2(b). Second, the potential of graphene on silicon is larger than that of suspended graphene, indicating that the contact with silicon or the strain from suspension influences the properties of graphene.

As we move from flat silicon to taller truncated silicon cones, graphene experiences increasing strain and reduced contact area. Graphene exposed to ambient conditions is p-doped with a distance to the Dirac point exceeding 65 meV, the maximum difference between the Schottky barrier heights of different devices. Thus, the abrupt change in the Schottky barrier from graphene/flat silicon to graphene/truncated silicon cones is likely due to the interfacial layer between graphene and silicon.

From G-TSC (H = 340 nm) to G-TSC (H = 720 nm), the increase of the Schottky barrier is mainly attributed to mechanical strain and dopants of graphene. According to previous studies, Fermi level (p-doped part) change within 50 meV could only change the Raman shift by a maximum of 2 cm^{-1} in the 2D peak [57]. Here, the downshift of the 2D peak is larger than 3 cm^{-1} compared to the graphene on flat silicon. Thus, the Raman shift is at least attributed to the introduced biaxial tensile strain in graphene from the symmetrical structure of truncated silicon cones, especially for nanocones with 720 nm

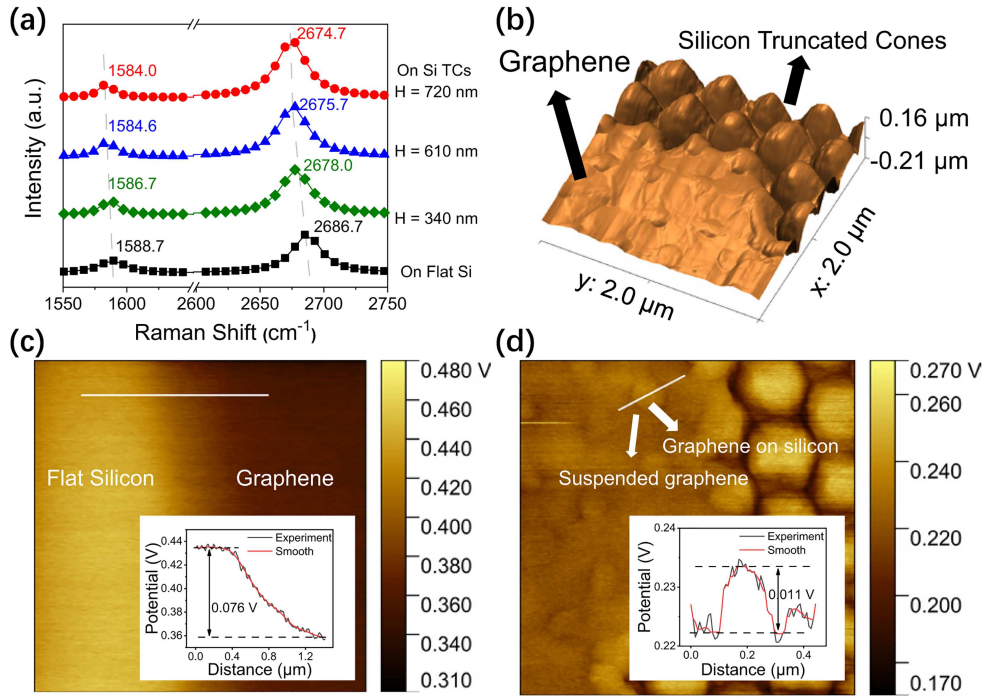

Figure 4 (Color online) Structural and interfacial characteristics Schottky barrier height. (a) Raman shift of graphene on four different structures; (b) 3-dimensional atomic force microscopy (AFM) image of graphene partially on silicon; (c) Kelvin probe force microscopy (KPFM) image of graphene partially on silicon; (d) KPFM image of the sample in (b). The insets show the line scan results.

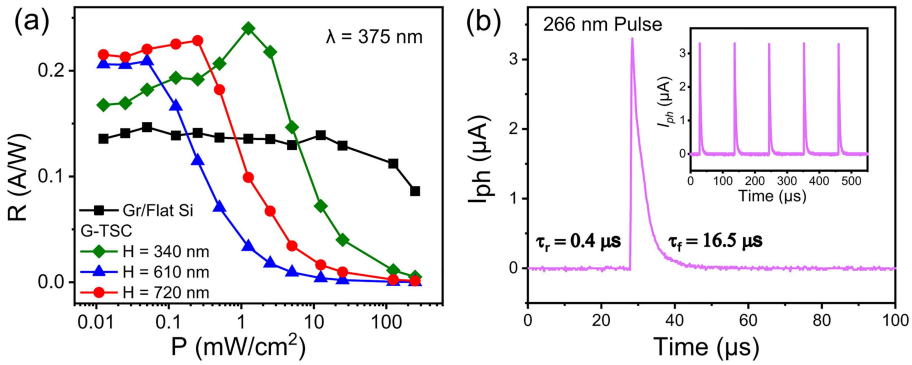

Figure 5 (Color online) Photoresponse. (a) Responsivity (@ −1 V) with different power density at 375 nm; (b) a single cycle photoresponse to pulsed 266 nm laser of the device (H = 720 nm) for estimating both rise time and fall time.

height. The related work points out that the shift of the G peak and the shift of the 2D peak will change in a similar ratio [58, 59, 71], while the experimental results show that the ratio between the two peaks is larger than expected. This suggests that dopants are also contributing to the Raman shift. The Fermi level of graphene will increase due to the increased strain and reduced contact area.

We suggest that the nanostructure could be further optimized or explored to get lower reflection. The inclination of the sidewall could be changed by adjusting the etching process, which provides more freedom for structural control of truncated nanocones. The fabrication of nanostructures is not limited by dry etching. It could also be metal-assisted chemical etching (MacEtch) or follow vapor-liquid-solid (VLS) growth for semiconductor nanowires [72–74].

We conducted assessments of dark current under reverse bias and noise power spectral density at −1 V for four device types in dark conditions, as depicted in Figures S3(b) and (c). As we previously discussed, lower truncated cones are associated with reduced barrier heights, and correspondingly, higher dark current density. The experimental data indeed confirms this trend, revealing that devices featuring lower truncated cones display a notably larger dark current. This implies that the tip area does not alter

the dark current density trend for truncated silicon cones in the context of this experiment. Besides, the dark current of G-TSC ($H = 720$ nm) can be lower than that of graphene/flat silicon photodetector.

Figure 5(a) shows the responsivity of G-TSC ($H = 720$ nm) with different power densities (375 nm) at -1 V bias. The responsivity of G-TSC is lower than that of graphene/flat silicon devices at higher light intensity. The increased light intensity has a similar effect on the device as a longer wavelength, evident in their shared influence on absorption depth. The volume of silicon at a certain thickness in G-TSC is less than that of bulk silicon. The surface recombination sites of G-TSC are more than that of the bulk silicon. It is worth mentioning that the sidewall surface area of G-TSC ($H = 610$ nm) is larger than that of G-TSC ($H = 720$ nm), which may explain the responsivity of G-TSC ($H = 610$ nm) decrease at a lower laser power.

The detectivity is next calculated using the data from Figure 5(a) and Figure S3(c) and plotted as shown in Figure S3(d).

$$D^* = \frac{\sqrt{A \cdot B}}{\text{NEP}} = \frac{\sqrt{A \cdot B}}{\sqrt{S_I}} \cdot R, \tag{1}$$

where A is the effective area of the detector, B is the bandwidth, NEP is the noise equivalent power, and S_I is the noise spectral density (NSD). Better detectivity cannot be guaranteed for lower reflection of the devices. Enhancing absorption around the junction area is more significant than simply reducing total reflection.

We also study the time response of G-TSC ($H = 720$ nm) using a 266 nm pulsed laser. In Figure 5(b), we present a single-cycle photoresponse, allowing for the estimation of both rise time (from 10% to 90% of the peak photocurrent) and fall time (from 90% to 10% of the peak photocurrent) at 0.4 and 16.5 μs, respectively. In contrast to other detectors, the G-TSC devices exhibit notably large responsivity at 360 nm, as shown in Table S1.

3 Conclusion

In summary, we have demonstrated a high-performance graphene-covered truncated silicon cone ultraviolet photodetector with an external quantum efficiency exceeding 113% at 360 nm by combined light-trapping, shallow junction, and impact ionization effects. The truncated silicon nanocones were fabricated to achieve a reflectivity below 12% in the 250 to 400 nm range. The fabrication process combines nanosphere lithography and ICP processing, offering simplicity, cost-effectiveness, and uniformity. Fabrication and analysis methods could also be applied to general low-dimensional materials/semiconductor nanostructures. Our framework offers a platform wherein Raman spectroscopy, KPFM analysis, and extraction of barrier height are instrumental in probing the physics mechanisms. It serves as a valuable tool for investigating photodetection performance and even two-dimensional material strain properties. In conclusion, graphene and truncated silicon nanocones-based photodetectors hold great promise for scalable and high quantum efficiency UV detection. Other low-dimensional materials and semiconductor nanostructures could also be used to further improve the performance.

4 Methods

4.1 Fabrication

A monolayer of polystyrene nanospheres (Beijing Zhongkeleiming, weight quality 10%, carboxyl-modified) with a diameter of 400 nm was deposited on the preprocessed silicon and reduced by Oxygen plasma (Diener, ZEPTO RIE). The truncated silicon cones were fabricated by ICP (Plasma pro100 Cobra 180, OXFORD) etching. Afterward, 1,1,2-trichlorotrifluoroethane (AR, 99%) was used to wash out the residue of polystyrene nanospheres. The CVD graphene (BGI) was transferred using the wet method, and the device was tilted to let it dry instead of blowing with N_2 when washing out the polymethyl methacrylate (PMMA). Last, devices were attached to the designed PCB board with gallium-indium and wire bonder (WE-2013).

4.2 Characterization

The reflectivity was measured by HITACHI U-4100 UV-Vis-NIR spectrometer at room temperature. SEM images were taken by ZEISS Gemini 300 and Crossbeam 350. Raman spectroscopy was measured by Renishaw inVia-Reflex. AFM and KPFM results were measured by Oxford MFP 3D.

4.3 Simulation

The electric field distribution was calculated by numerically solving Maxwell's equations under the normal incidence of light using the commercial software COMSOL Multiphysics 5.6. The wave vector of the incident light was perpendicular to the interface, and its polarization was perpendicular to the edge of the hexagonal lattice. The refractive index of the silicon substrate was obtained from [75] and a typical mesh size (approximately 0.5 nm) was used.

4.4 Measurement

A broadband light source with a monochromator was used to characterize the response with different wavelengths. The electrical measurements and noise were performed using a source meter (Keithley 2450 and 2636) and a semiconductor analyzer (PDA FS480). The 266 nm laser operates with a pulse duration of 1.3 ns and offers single pulse energy output between 0.1 to 3 μJ. The time response was characterized by a Transimpedance Amplifier (FEMTO HAS-Y-2-40) and an oscilloscope (RIGOL MSO8104) with 375 and 532 nm laser modulated by a signal generator (RIGOL DG5101).

Acknowledgements This work was supported by National Key R&D Program of China (Grant No. 2022YFA1204304), National Natural Science Foundation of China (Grant No. U22A2076), Zhejiang Provincial Young Talents Program, Natural Science Foundation of Zhejiang Province (Grant No. LDT23F04013F04), and China Scholarship Council (Grant No. 202106320210). We thank Dr. Yiwei SUN, Chenhao WANG, Dr. Lingfei LI, Dr. Wei LIU, Dr. Jianhang LV, and Dr. Hongwei GUO for their valuable discussions and assistance. The authors thank the support of the nanofabrication facility in ZJU-UIUC Institute as well as the Micro/Nano Fabrication Center of Zhejiang University.

Supporting information Figures S1–S4 and Table S1. The supporting information is available online at info.scichina.com and link.springer.com. The supporting materials are published as submitted, without typesetting or editing. The responsibility for scientific accuracy and content remains entirely with the authors.

References

1 Alaie Z, Nejad S M, Yousefi M H. Recent advances in ultraviolet photodetectors. Mater Sci Semicond Process, 2015, 29: 16–55
2 Razeghi M, Rogalski A. Semiconductor ultraviolet detectors. J Appl Phys, 1996, 79: 7433–7473
3 Shi L, Nihtianov S. Comparative study of silicon-based ultraviolet photodetectors. IEEE Sens J, 2012, 12: 2453–2459
4 Chen H, Liu K, Hu L, et al. New concept ultraviolet photodetectors. Mater Today, 2015, 18: 493–502
5 Chen H, Liu H, Zhang Z, et al. Nanostructured photodetectors: from ultraviolet to Terahertz. Adv Mater, 2016, 28: 403–433
6 Peng L, Hu L, Fang X. Low-dimensional nanostructure ultraviolet photodetectors. Adv Mater, 2013, 25: 5321–5328
7 Monroy E, Omnès F, Calle F. Wide-bandgap semiconductor ultraviolet photodetectors. Semicond Sci Technol, 2003, 18: R33–R51
8 Wan X, Xu Y, Guo H, et al. A self-powered high-performance graphene/silicon ultraviolet photodetector with ultra-shallow junction: breaking the limit of silicon? npj 2D Mater Appl, 2017, 1: 4
9 Zou Y, Zhang Y, Hu Y, et al. Ultraviolet detectors based on wide bandgap semiconductor nanowire: a review. Sensors, 2018, 18: 2072
10 Omnés F, Monroy E, Muñoz E et al. Wide bandgap UV photodetectors: a short review of devices and applications. In: Proceedings of SPIE, 2007. 64730E
11 BenMoussa A, Soltani A, Schühle U, et al. Recent developments of wide-bandgap semiconductor based UV sensors. Diamond Relat Mater, 2009, 18: 860–864
12 Wang Q, Savage S, Noharet B, et al. Analysis and comparison of UV photodetectors based on wide bandgap semiconductors. In: Proceedings of SPIE, 2010. 760225
13 Sze S M, Ng K K. Physics of Semiconductor Devices. 3rd ed Hoboken: Wiley-Interscience, 2007
14 Green M A, Keevers M J. Optical properties of intrinsic silicon at 300 K. Prog Photovoltaics, 1995, 3: 189–192
15 Green M A. Self-consistent optical parameters of intrinsic silicon at 300K including temperature coefficients. Sol Energy Mater Sol Cells, 2008, 92: 1305–1310
16 Blacksberg J, Nikzad S, Hoenk M E, et al. Near-100% quantum efficiency of delta doped large-format UV-NIR silicon imagers. IEEE Trans Electron Devices, 2008, 55: 3402–3406
17 Li X, Zhu H, Wang K, et al. Graphene-on-silicon Schottky junction solar cells. Adv Mater, 2010, 22: 2743–2748
18 Chen C C, Aykol M, Chang C C, et al. Graphene-silicon Schottky diodes. Nano Lett, 2011, 11: 1863–1867
19 Bartolomeo A D, Luongo G, Iemmo L, et al. Graphene-silicon Schottky diodes for photodetection. IEEE Trans Nanotechnol, 2018, 17: 1133–1137
20 Li X, Zhu M, Du M, et al. High Detectivity Graphene-silicon heterojunction photodetector. Small, 2016, 12: 595–601
21 Sinha D, Lee J U. Ideal Graphene/silicon Schottky junction diodes. Nano Lett, 2014, 14: 4660–4664

22 An Y, Behnam A, Pop E, et al. Metal-semiconductor-metal photodetectors based on graphene/*p*-type silicon Schottky junctions. Appl Phys Lett, 2013, 102: 013110

23 Wang L, Ren Z F, Wang K Y, et al. Graphene-pyramid textured silicon heterojunction for sensitive near-infrared light photodiode. Mater Res Express, 2017, 4: 045022

24 Zeng L, Han W, Wu S E, et al. Graphene/$PtSe_2$/Pyramid Si van Der Waals Schottky junction for room-temperature broadband infrared light detection. IEEE Trans Electron Devices, 2022, 69: 6212–6216

25 Xiao P, Mao J, Ding K, et al. Solution-processed 3D RGO-MoS_2/Pyramid Si heterojunction for ultrahigh detectivity and ultra-broadband photodetection. Adv Mater, 2018, 30: 1801729

26 Zhao J, Liu H, Deng L, et al. High quantum efficiency and broadband photodetector based on graphene/silicon nanometer truncated cone arrays. Sensors, 2021, 21: 6146

27 Yang J, Tang L, Luo W, et al. Light trapping in conformal graphene/silicon nanoholes for high-performance photodetectors. ACS Appl Mater Interfaces, 2019, 11: 30421–30429

28 Fan G, Zhu H, Wang K, et al. Graphene/silicon nanowire Schottky junction for enhanced light harvesting. ACS Appl Mater Interfaces, 2011, 3: 721–725

29 Zhang X, Xie C, Jie J, et al. High-efficiency graphene/Si nanoarray Schottky junction solar cells via surface modification and graphene doping. J Mater Chem A, 2013, 1: 6593

30 Feng B, Pan X, Liu T, et al. A broadband photoelectronic detector in a silicon nanopillar array with high detectivity enhanced by a monolayer graphene. Nano Lett, 2021, 21: 5655–5662

31 Feng T, Xie D, Lin Y et al. Graphene based Schottky junction solar cells on patterned silicon-pillar-array substrate. Appl Phys Lett, 2011, 99: 233505

32 Kim J, Joo S S, Lee K W, et al. Near-ultraviolet-sensitive graphene/porous silicon photodetectors. ACS Appl Mater Interfaces, 2014, 6: 20880–20886

33 Luongo G, Grillo A, Giubileo F, et al. Graphene Schottky junction on pillar patterned silicon substrate. Nanomaterials, 2019, 9: 659

34 Bartolomeo A D, Giubileo F, Luongo G, et al. Tunable Schottky barrier and high responsivity in graphene/Si-nanotip optoelectronic device. 2D Mater, 2016, 4: 015024

35 Pan S, Wu S E, Hei J, et al. Light trapping enhanced broadband photodetection and imaging based on $MoSe_2$/pyramid Si vdW heterojunction. Nano Res, 2023, 16: 10552–10558

36 Wu D, Jia C, Shi F, et al. Mixed-dimensional $PdSe_2$/SiNWA heterostructure based photovoltaic detectors for self-driven, broadband photodetection, infrared imaging and humidity sensing. J Mater Chem A, 2020, 8: 3632–3642

37 Zeng L, Lin S, Lou Z, et al. Ultrafast and sensitive photodetector based on a $PtSe_2$/silicon nanowire array heterojunction with a multiband spectral response from 200 to 1550 nm. NPG Asia Mater, 2018, 10: 352–362

38 Wang J J, Fu C, Cheng H Y, et al. Leaky mode resonance-induced sensitive ultraviolet photodetector composed of graphene/small diameter silicon nanowire array heterojunctions. ACS Nano, 2021, 15: 16729–16737

39 Garin M, Heinonen J, Werner L, et al. Black-silicon ultraviolet photodiodes achieve external quantum efficiency above 130%. Phys Rev Lett, 2020, 125: 117702

40 Hulteen J C, van Duyne R P. Nanosphere lithography: a materials general fabrication process for periodic particle array surfaces. J Vacuum Sci Tech A-Vacuum Surfs Films, 1995, 13: 1553–1558

41 Haynes C L, van Duyne R P. Nanosphere lithography: a versatile nanofabrication tool for studies of size-dependent nanoparticle optics. J Phys Chem B, 2001, 105: 5599–5611

42 Whitney A V, Myers B D, van Duyne R P. Sub-100 nm triangular nanopores fabricated with the reactive ion etching variant of nanosphere lithography and angle-resolved nanosphere lithography. Nano Lett, 2004, 4: 1507–1511

43 Tielrooij K J, Song J C W, Jensen S A, et al. Photoexcitation cascade and multiple hot-carrier generation in graphene. Nat Phys, 2013, 9: 248–252

44 Ma Q, Andersen T I, Nair N L, et al. Tuning ultrafast electron thermalization pathways in a van der Waals heterostructure. Nat Phys, 2016, 12: 455–459

45 Brongersma M L, Halas N J, Nordlander P. Plasmon-induced hot carrier science and technology. Nat Nanotech, 2015, 10: 25–34

46 Juntunen M A, Heinonen J, Vähänissi V, et al. Near-unity quantum efficiency of broadband black silicon photodiodes with an induced junction. Nat Photon, 2016, 10: 777–781

47 Vavilov V S. Effects of Radiation on Semiconductors. Boston: Springer US, 1965

48 Vavilov V S. Radiation ionization processes in germanium and silicon crystals. Sov Phys Usp, 1962, 4: 761–769

49 Maes W, Meyer K D, van Overstraeten R. Impact ionization in silicon: a review and update. Solid-State Electron, 1990, 33: 705–718

50 Shockley W. Problems related to p-n junctions in silicon. Solid-State Electron, 1961, 2: 35–67

51 Kolodinski S, Werner J H, Wittchen T, et al. Quantum efficiencies exceeding unity due to impact ionization in silicon solar cells. Appl Phys Lett, 1993, 63: 2405–2407

52 Kumaravelu G, Alkaisi M M, Bittar A, et al. Damage studies in dry etched textured silicon surfaces. Curr Appl Phys, 2004, 4: 108–110

53 Wu W, McLarty P K. Reactive ion etching induced damage with gas mixtures CHF_3/O_2 and SF_6/O_2. J Vac Sci Tech, 1995, 13: 67–72

54 Liu X, Radfar B, Chen K, et al. Tailoring femtosecond-laser processed black silicon for reduced carrier recombination combined with >95% above-bandgap absorption. Adv Photonics Res, 2022, 3: 2100234

55 Oehrlein G S. Dry etching damage of silicon: a review. Mater Sci Eng-B, 1989, 4: 441–450

56 Cheung S K, Cheung N W. Extraction of Schottky diode parameters from forward current-voltage characteristics. Appl Phys Lett, 1986, 49: 85–87

57 Das A, Pisana S, Chakraborty B, et al. Monitoring dopants by Raman scattering in an electrochemically top-gated graphene

transistor. Nat Nanotech, 2008, 3: 210–215
58 Jie W, Yu Hui Y, Zhang Y, et al. Effects of controllable biaxial strain on the Raman spectra of monolayer graphene prepared by chemical vapor deposition. Appl Phys Lett, 2013, 102: 223112
59 Ding F, Ji H, Chen Y, et al. Stretchable graphene: a close look at fundamental parameters through biaxial straining. Nano Lett, 2010, 10: 3453–3458
60 Choi S M, Jhi S H, Son Y W. Effects of strain on electronic properties of graphene. Phys Rev B, 2010, 81: 081407
61 Klimov N N, Jung S, Zhu S, et al. Electromechanical properties of graphene drumheads. Science, 2012, 336: 1557–1561
62 Hwang C, Siegel D A, Mo S K, et al. Fermi velocity engineering in graphene by substrate modification. Sci Rep, 2012, 2: 590
63 Reserbat-Plantey A, Kalita D, Han Z, et al. Strain superlattices and macroscale suspension of graphene induced by corrugated substrates. Nano Lett, 2014, 14: 5044–5051
64 Gill S T, Hinnefeld J H, Zhu S, et al. Mechanical control of graphene on engineered pyramidal strain arrays. ACS Nano, 2015, 9: 5799–5806
65 Si C, Sun Z, Liu F. Strain engineering of graphene: a review. Nanoscale, 2016, 8: 3207–3217
66 Hinnefeld J H, Gill S T, Mason N. Graphene transport mediated by micropatterned substrates. Appl Phys Lett, 2018, 112: 173504
67 Dai Z, Liu L, Zhang Z. Strain engineering of 2D materials: issues and opportunities at the interface. Adv Mater, 2019, 31: 1805417
68 Pu D, Anwar M A, Zhou J, et al. Enhanced photovoltaic effect in graphene C silicon Schottky junction under mechanical manipulation. Appl Phys Lett, 2023, 122: 041102
69 Song Y, Li X, Mackin C, et al. Role of interfacial oxide in high-efficiency graphene C silicon Schottky barrier solar cells. Nano Lett, 2015, 15: 2104–2110
70 Yoon H H, Jung S, Choi G, et al. Strong fermi-level pinning at Metal/n-Si(001) interface ensured by forming an intact Schottky contact with a graphene insertion layer. Nano Lett, 2017, 17: 44–49
71 del Corro E, Taravillo M, Baonza V G. Nonlinear strain effects in double-resonance Raman bands of graphite, graphene, and related materials. Phys Rev B, 2012, 85: 033407
72 Fortuna S A, Li X. Metal-catalyzed semiconductor nanowires: a review on the control of growth directions. Semicond Sci Technol, 2010, 25: 024005
73 Li X. Metal assisted chemical etching for high aspect ratio nanostructures: a review of characteristics and applications in photovoltaics. Curr Opin Solid State Mater Sci, 2012, 16: 71–81
74 Zhang C, Miao X, Mohseni P K, et al. Site-controlled VLS growth of planar nanowires: yield and mechanism. Nano Lett, 2014, 14: 6836–6841
75 Pierce D T, Spicer W E. Electronic structure of amorphous si from photoemission and optical studies. Phys Rev B, 1972, 5: 3017–3029